Link to publisher's version: *http://dx.doi.org/10.1016/j.compfluid.2015.03.010*

Citation: Pu JH (2015) Turbulence modelling of shallow water flows using Kolmogorov approach. Computers and Fluids. 115: 66-74.

Turbulence Modelling of Shallow Water Flows Using Kolmogorov Approach

JAAN HUI PU

Lecturer, School of Engineering, Faculty of Engineering and Informatics, University of Bradford, Bradford DB7 1DP, UK.

(*Visiting Scientist, State Key Laboratory of Hydro-Science and Engineering, Tsinghua University, Beijing 100084, China*)

Email: j.h.pu1@bradford.ac.uk

ABSTRACT

This study uses an improved k-ε coupled shallow water equations (SWE) model that equipped with the numerical computation of the velocity fluctuation terms to investigate the turbulence structures of the open channel flows. We adapted the Kolmogorov K41 scaling model into the k-ε equations to calculate the turbulence intensities and Reynolds stresses of the SWE model. The presented model was also numerically improved by a recently proposed surface gradient upwind method (SGUM) to allow better accuracy in simulating the combined source terms from both the SWE and k-ε equations as proven in the recent studies. The proposed model was first tested using the flows induced by multiple obstructions to investigate the utilised k-ε and SGUM approaches in the model. The laboratory experiments were also conducted under the non-uniform flow conditions, where the simulated velocities, total kinetic energies (TKE) and turbulence intensities by the proposed model were used to compare with the measurements under different flow non-uniformity conditions. Lastly, the proposed numerical simulation was compared with a standard Boussinesq model to investigate its capability to simulate the measured Reynolds stress. The comparison outcomes showed that the proposed Kolmogorov k-ε SWE model can capture the flow turbulence characteristics reasonably well in all the investigated flows.

Keywords: Kolmogorov K41 scaling law; SGUM model; SWE k-ε model; non-uniform flow experiment; Reynolds stress; turbulence structures

1 Introduction

In order to simulate the turbulence structures in various flow conditions, the full 3D Navier Stokes (NS) numerical models are usually used (e.g., in Liu and Garcia [1] and Bihs and Olsen [2]). There are several 3D NS modelling numerical methods discovered in the recent decades that can be used to capture the free surface flow characteristics, namely the Marker and Cell (by Harlow and Welch [3]), the Volume of Fluid (by Lin and Liu [4]), the Arbitrary Lagrangian Eulerian (by Zhou and Stansby [5]) and the Level-Set methods (by Iafrati et al. [6]). However, the numerical simulation of the 3D NS equations to resolve the flow turbulence characteristics usually demands high computational cost, which strongly restricts its application in practical engineering aspects. There are two main reasons for that: (1) turbulent flows usually involve extensive and complex spatial domain evolution with very fine numerical meshes needed, and (2) those flows usually have very unsteady numerical wave speeds and that couple with small meshing areas will limit the maximum computational time step that can be employed to achieve accurate turbulent flow results. In the view of these reasons, the search for more computationally efficient model is crucial to achieve practical turbulent characteristics representation in various water engineering applications.

In the more computationally effective 2D turbulence structures representation, some complex numerical models, such as the direct numerical simulation – DNS model [7] and large-eddy simulation – LES model [8], has been studied due to their previous success in simulating the 3D NS flows. Despite their high computational costs, their success has been restrained by the meshing control and tracking of turbulence eddies break-down, which subsequently contributed to their employment of high demanding numerical approaches. Other way to model the flow turbulence intensity or Reynolds stress in Reynolds Averaged Navier Stokes (RANS) model is by using the Reynolds stress-type model (RSM), such as the non-linear RSM model suggested by Shih et al. [9]. From the complex closure formulation of the RSM equations, it can be observed that the model is more computationally expensive than the k-type models, such as the k-ε model (refer to the studies by Rodi [10]; and more recently by Cea [11]; Jiang et al. [12] and Pu et al. [13]), and by employing the RSM model might defeat the purpose to create a computationally practical model.

Compared to the usual way of turbulence modelling by 3D NS model, the RANS type of Shallow Water Equations (SWE) model is more numerically efficient. However, there is a challenge to implement the numerical calculation of the turbulent intensity and Reynolds stress into the SWE model due to its Reynolds decomposed feature that discounts the velocity fluctuation terms in all directions. The comparative study on various numerical models conducted by Cea et al. [14,15] has proven that the 2D depth-averaged turbulence models can combine with the SWE model to give reasonable representation to flow turbulence structures in shallow flow condition. Inspired by them, this study implemented the Kolmogorov K41 scaling model (originally suggested by Kolmogorov [16-18] and normally used to represent flow power spectrum such as in Pu et al. [13]; Nezu and Nakagawa [19]; and Hunt et al. [20]) into the k-ε equations to describe a new model that can be combined with the SWE model to give efficient turbulent structures simulation. The new model is efficient because: (1) its SWE simulates only 2D flow conditions, and (2) its velocity fluctuations are not represented by any complicated strain rate or vorticity tensor (as in the normal RSM and Boussinesq approaches), but instead are computed by the Kolmogorov method.

As highlighted by the studies of Caselles et al. [21], Fernandez-Nieto et al. [22] and Xia et al. [23] using different numerical models and schemes, the numerical source terms are crucial to be treated in well-balanced manner for the complex flow modelling, especially for the turbulent flow induced from obstruction and complex geometry. Hence, a recently proposed surface gradient upwind method (SGUM) by Pu et al. [24] was used in this study to improve the numerical source term simulations by integrating them into the main upwind scheme commonly used to update the numerical flux terms. The utilised SGUM approach integrated the combined source terms from the SWE and k-ε equations into a monotonic upwind-Hancock (MUSCL-Hancock) scheme for the numerical fluxes and improved the simulation accuracy of the flow turbulence structures. To this end, the newly proposed numerical model has been improved in both its modelling approach and numerical method.

In order to verify the proposed model, both the obstruction induced flows and experimentally investigated non-uniform flows were used to compare with the model. In the obstructed flows investigation, a complex multiple-block obstructions induced flow study in literature was used to compare with the proposed model simulations. Furthermore, a laboratory experiment was also conducted under different non-uniform flow conditions to validate the presented model. Four different flow non-uniformity conditions were considered in our experiment, and multiple measurements at separate flow locations were taken for each non-uniform flow. All the flow experiments were conducted using the physical water flume facility located in the Hydraulic Laboratory at the University of Bradford (refer to Pu et al. [13] and Pu [25]).

The comparisons between the numerical, experimental as well as literature studies showed that the proposed model can simulate the flow turbulence structures reasonably well for all the investigated flow conditions. These comparisons showed that the proposed model successfully combines the k-ε and Kolmogorov approaches into the 2D SWE model to efficiently re-generate the flow turbulence structures that are lost during the Reynolds decomposition process, which it represents an important numerical modelling aspect for simulating open channel flow applications in a practical manner.

2 Shallow Water Equations (SWE) Model

The SWE model is used to couple with the k-ε turbulence model in this study. Equations (1) – (3) present the 2D fully conservative SWE, and it is combined with the numerical flux terms from the k-ε model.

$$\frac{\partial \phi}{\partial t}+\frac{\partial \phi u}{\partial x}+\frac{\partial \phi v}{\partial y}=0 \tag{1}$$

$$\frac{\partial \phi u}{\partial t}+\frac{\partial\left(\phi u^2+\phi^2/2\right)}{\partial x}+\frac{\partial \phi uv}{\partial y}-\frac{\partial}{\partial x}\left[2\nu_t\frac{\partial(\phi u)}{\partial x}-\frac{2}{3}\phi k\right]-\frac{\partial}{\partial y}\left[\nu_t\left(\frac{\partial(\phi u)}{\partial y}+\frac{\partial(\phi v)}{\partial x}\right)\right]$$
$$=g\phi\left(S_{ox}-S_{fx}\right) \tag{2}$$

$$\frac{\partial \phi v}{\partial t}+\frac{\partial \phi uv}{\partial x}+\frac{\partial\left(\phi v^2+\phi^2/2\right)}{\partial y}-\frac{\partial}{\partial x}\left[\nu_t\left(\frac{\partial(\phi u)}{\partial y}+\frac{\partial(\phi v)}{\partial x}\right)\right]-\frac{\partial}{\partial y}\left[2\nu_t\frac{\partial(\phi v)}{\partial y}-\frac{2}{3}\phi k\right]$$
$$=g\phi\left(S_{oy}-S_{fy}\right) \tag{3}$$

In the equations above, the variable ϕ refers to geopotential and is given by $\phi = g\cdot h$, where h is the water depth and g is the gravitational acceleration. u and v are the depth averaged flow velocities in streamwise and lateral directions, respectively. k is the flow turbulent kinetic energy (TKE), and the depth-averaged turbulent viscosity ν_t is calculated as $\nu_t = C_\mu k^2/\varepsilon$, where C_μ is the turbulence viscosity coefficient (used in this study as $C_\mu = 0.09$) and ε is the flow TKE dissipation rate. x, y and t denote the spatial-longitudinal, spatial-lateral and temporal domains, respectively.

In equations (2) and (3), S_{ox} and S_{oy} are the bed slopes in the streamwise and lateral directions, respectively. For the friction slope of the channel S_f, they are computed as follows

$$S_{fx}=\frac{n^2u\sqrt{u^2+v^2}}{h^{4/3}}, \text{ and } S_{fy}=\frac{n^2v\sqrt{u^2+v^2}}{h^{4/3}} \tag{4}$$

where n is the Manning's friction coefficient.

3 Turbulence Model Implementation

The 2D k-ε equations coupled with the SWE model are presented below [25,26]

$$\frac{\partial \phi k}{\partial t}+\frac{\partial \phi uk}{\partial x}+\frac{\partial \phi vk}{\partial y}-\frac{\partial}{\partial x}\left[\frac{\nu_t}{\sigma_k}\cdot\frac{\partial(\phi k)}{\partial x}\right]-\frac{\partial}{\partial y}\left[\frac{\nu_t}{\sigma_k}\cdot\frac{\partial(\phi k)}{\partial y}\right]=g\cdot R_h+g\cdot R_k-\phi\varepsilon \tag{5}$$

$$\frac{\partial \phi \varepsilon}{\partial t}+\frac{\partial \phi u\varepsilon}{\partial x}+\frac{\partial \phi v\varepsilon}{\partial y}-\frac{\partial}{\partial x}\left[\frac{\nu_t}{\sigma_\varepsilon}\cdot\frac{\partial(\phi \varepsilon)}{\partial x}\right]-\frac{\partial}{\partial y}\left[\frac{\nu_t}{\sigma_\varepsilon}\cdot\frac{\partial(\phi \varepsilon)}{\partial y}\right]=\frac{\varepsilon}{k}\left(g\cdot C_1\cdot R_h-C_2\cdot\phi\varepsilon\right)+g\cdot R_\varepsilon \tag{6}$$

Each of the parameters R_h, R_k, and R_ε in equations (5) and (6) can be represented as

$$R_h = \frac{\nu_t}{z}\left\{2\left[\frac{\partial(hu)}{\partial x}\right]^2 + 2\left[\frac{\partial(hv)}{\partial y}\right]^2 + \left[\frac{\partial(hu)}{\partial y} + \frac{\partial(hv)}{\partial x}\right]^2\right\}, R_k = \frac{n^2 g}{h^{\frac{1}{3}}}\left(u^2+v^2\right)^{\frac{3}{2}}, \text{ and}$$

$$R_\varepsilon = \frac{C_2 C_\mu n^{\frac{5}{2}} g^{\frac{5}{4}} \left(u^2+v^2\right)^2}{h^{\frac{17}{12}}} \tag{7}$$

The turbulence parameters used in equations (5) – (7) are $C_1 = 1.432$, $C_2 = 1.913$, $\sigma_k = 0.990$, and $\sigma_\varepsilon = 1.290$ (refer to the study by Pu et al. [13]). By using the combination of the above k-ε turbulence model with the Kolmogorov's [16-18] law in estimating velocity fluctuations, we can compute the turbulence structures, including turbulence intensity and Reynolds stress, for the proposed model.

Adapting the derived equation from the Kolmogorov K41 scaling law used in Nezu and Nakagawa [19] and Hunt et al. [20], the streamwise velocity fluctuation can be described in our numerical computation as

$$(u')_i^N = \sqrt[3]{\frac{(\varepsilon)_i^N \cdot (L_x)_i^N}{k_L}} \tag{8}$$

where i and N represent the numerical simulation space and time steps, respectively. u' is the fluctuation of the streamwise velocity (which represents turbulence intensity in x-direction), L_x is the macroscale of turbulence, and k_L is the turbulence coefficient that can be calculated by equation (9). In equation (8), the numerical main-stream (streamwise) velocity fluctuation was calculated by a relationship between the numerically calculated ε and comparative parameter L_x.

$$k_L = \left[2/\left(\pi C_k\right)\right]^{3/2} \alpha^{5/2} \tag{9}$$

In equation (9), C_k is a universal constant varies from 0.45 to 0.55. α is a dimensionless parameter defined as $\alpha = L_x k_0$ in which the reciprocal k_0^{-1} is also a macroscale of turbulence, as the same as L_x.

Hence, this study adopted the suggestion of Nezu and Nakagawa [19] in its numerical calculations, where α was estimated to be in the order of unity. The macroscale of turbulence L_x in equation (8) can be calculated by the Kolmogorov microscale of turbulence η_k as

$$\left(L_x\right)_i^N = 0.91Re^{3/4}\left(\eta_k\right)_i^N \tag{10}$$

where

$$\left(\eta_k\right)_i^N = \left[\frac{{\nu_k}^3}{\left(\varepsilon\right)_i^N}\right]^{1/4} \tag{11}$$

in which, Re is the Reynolds number; and ν_k is the kinematic viscosity of flow.

As an extension towards the mixing length theory proposed by Prandtl in 1945 to describe the dominant eddies mixing process, the turbulent kinetic energy (TKE) can be usually represented by the velocity fluctuations in different directions [19]. In our SWE model, due to the absent of vertical velocity fluctuation through depth-averaging, the numerically computed k could be estimated as

$$\left(k\right)_i^N = \frac{1}{2}\left[\left(u'^2\right)_i^N + \left(v'^2\right)_i^N\right] \tag{12}$$

where v' is the lateral velocity fluctuation (turbulence intensity in y-direction). Combining the streamwise turbulent intensity calculated using Kolmogorov approach in equation (8) and the computed k from k-ε equations (5) and (6) into equation (12), we can estimate the lateral turbulent intensity as well as u-v Reynolds stress to fully study the flow turbulence structures. The Kolmogorov model used in this study computes separate streamwise and lateral turbulent intensities before combining them to calculate the u-v Reynolds stress; and by this way it provides addition turbulent intensity information to investigate the flow turbulence structures. Since the Kolmogorov model calculates separate turbulent intensities for different directions, it can also be easily converted to use in 1D model or to extend to consider flow turbulence structures in 3D model with appropriate assumptions. However, the current Kolmogorov approach extension to 3D model should be done in caution as the 3D consideration will increase the computational cost as compared to the current 2D SWE approach, and this will hinder the practicality of the model.

Also worth noting that the utilised k-ε model in equations (5) – (6) is valid under turbulent flow Reynolds number as suggested by Rodi [10] and Cea [11]. Its applications into various shallow flow cases have been tested by Cea [11]; Jiang et al. [12] and Younus and Chaudhry [27] for its validity on flows under different velocity and uniformity. For the Kolmogorov method used in this study, it is valid to represent turbulent structures in wide open channel flows as suggested by Nezu and Nakagawa [19]. Besides the method also showed stable characteristics towards the turbulent Reynolds number flow case, which this stable results was showing when k_L in equation (9) was tested against Reynolds number [19]. Thus from these two separate findings on the SWE k-ε model and Kolmogorov method, this study suggests their combination to calculate the shallow water turbulence structures, which has been lost through the Reynolds decomposition process.

4 Numerical Schemes

In this study, the numerical flux terms were discretized using a Godunov-type Hancock scheme. The Hancock scheme was upgraded by a two-stage predictor-corrector time-stepping approach. A standard Harten Lax van Leer-contact (HLLC) approximate Riemann solver was used to couple with the Hancock scheme for the Riemann data reconstruction process. The slope limiter method was used in the HLLC solver to ensure the space discretization scheme satisfies the flux-limiting property [28-30]. The source term of the proposed numerical scheme was modelled using a surface gradient upwind method (SGUM) proposed by Pu et al. [24].

The Godunov-type scheme was used in this study as it has been proven in Toro [28] and Toro and Garcia-Navarro [31] to show good capability to resolve the discontinuous condition in various shallow flow applications. This criterion is important for us to model the flow turbulence with discontinuities and shocks under the shallow flow condition. Besides, the combination of HLLC approximate Riemann solver with Godunov-type scheme has been proven by Toro [28] to be numerically well-fitted together by causing least spurious oscillations when compared to Reo or HLL solvers. Due to all these reasons, the full Godunov-type HLLC approximate Riemann numerical formulation is used in this study to simulate the flow turbulence in shallow water applications.

To ease the numerical representation, equations (1) – (3) and (5) – (6) are combined into a single vector operation as follows

$$\frac{\partial \mathbf{U}}{\partial t} + \nabla \cdot \mathbf{F} = \mathbf{S_T} \tag{13}$$

where

$$\mathbf{U} = \begin{bmatrix} \phi \\ \phi u \\ \phi v \\ \phi k \\ \phi \varepsilon \end{bmatrix}, \mathbf{F} = \begin{bmatrix} \phi u_t \\ \phi u u_t + \frac{\phi}{2}\left(\phi + \frac{4}{3}k\right) - 2\nu_t \cdot \left(\nabla_x \cdot (\phi u_t) + \nabla_y \cdot \left(\frac{\phi u}{2}\right)\right) \\ \phi v u_t + \frac{\phi}{2}\left(\phi + \frac{4}{3}k\right) - 2\nu_t \cdot \left(\nabla_y \cdot (\phi u_t) + \nabla_x \cdot \left(\frac{\phi v}{2}\right)\right) \\ \frac{\nu_t}{\sigma_k} \cdot \nabla \cdot (\phi k) \\ \frac{\nu_t}{\sigma_\varepsilon} \cdot \nabla \cdot (\phi \varepsilon) \end{bmatrix}, \mathbf{S_T} = \begin{bmatrix} 0 \\ g\phi\left(S_{ox} - S_{fx}\right) \\ g\phi\left(S_{oy} - S_{fy}\right) \\ g \cdot P_h + g \cdot P_k - \phi\varepsilon \\ \frac{\varepsilon}{k}\left(g \cdot C_1 \cdot P_h - C_2 \cdot \phi\varepsilon\right) + g \cdot P_\varepsilon \end{bmatrix} \tag{14}$$

$\mathbf{U}$, $\mathbf{F}$ and $\mathbf{S_T}$ in equations (13) and (14) represent the matrices for the flow conserved variables, numerical flux and source terms, respectively; u_t is the resultant velocity defined by $u_t = \sqrt{u^2 + v^2}$; and ∇ is the gradient operator that can be expressed as $\nabla = \nabla_x + \nabla_y$, where $\nabla_x = \mathbf{i} \cdot \partial / \partial x$ and $\nabla_y = \mathbf{j} \cdot \partial / \partial y$. $\mathbf{i}$ and $\mathbf{j}$ are the unit vectors in x- and y-directions, respectively.

4.1 *Monotone Upwind–Hancock Scheme*

In our employed monotonic upwind scheme for conservative laws (MUSCL), the data reconstruction process of the flow conserved variables vector gives [28]

$$\mathbf{U}_{i+1/2}^{L} = \mathbf{U}_i - \frac{\Pi(q_i)\cdot\Delta\mathbf{U}_{i-1/2}}{2}, \text{ and, } \mathbf{U}_{i+1/2}^{R} = \mathbf{U}_{i+1} + \frac{\Pi(q_{i+1})\cdot\Delta\mathbf{U}_{i+1/2}}{2} \tag{15}$$

where $q_i = \frac{\Delta\mathbf{U}_{i+1/2}}{\Delta\mathbf{U}_{i-1/2}}$, $q_{i+1} = \frac{\Delta\mathbf{U}_{i+3/2}}{\Delta\mathbf{U}_{i+1/2}}$, $\Delta\mathbf{U}_{i+1/2} = \mathbf{U}_{i+1} - \mathbf{U}_i$, and $\Delta\mathbf{U}_{i-1/2} = \mathbf{U}_i - \mathbf{U}_{i-1}$ (16)

where Π is the slope limiter; and q is the gradient of successive $\Delta\mathbf{U}$. The van Leer's limiter, which proposed and tested by van Leer [32] into the MUSCL scheme, has been used in equation (15). As suggested by the numerical tests of Toro [28] and Hu et al. [30], the van Leer's limiter gives the best converged result to the analytical solution as compared with various other slope limiters; hence it is employed in this study.

A Hancock two-stage predictor-corrector scheme was utilised to update $\mathbf{U}$ across the time domain in the proposed explicit model. Unlike some common numerical schemes, e.g. the weighted average flux (WAF) and first-order centred (FORCE) schemes that use the Lax-Wendroff (LW) and slope limiter centred (SLIC) methods, respectively, the MUSCL-Hancock scheme reconstructs its solution through the piece-wise linear functions that depend on values extrapolated from time-evolving boundary conditions [28]. In this way, the MUSCL-Hancock scheme can achieve second order accuracy in the spatial and temporal domains while maintains its stability.

The predictor-corrector steps are given as [29,30]

Predictor Step: $$\mathbf{U}_i^{N+1/2} = \mathbf{U}_i^N - \frac{\Delta t}{2\Omega_i}\left(\mathbf{F}_{i+1/2}^N - \mathbf{F}_{i-1/2}^N\right) \tag{17}$$

Corrector Step: $$\mathbf{U}_i^{N+1} = \mathbf{U}_i^N - \frac{\Delta t}{\Omega_i}\left(\mathbf{F}_{i+1/2}^{N+1/2} - \mathbf{F}_{i-1/2}^{N+1/2}\right) \tag{18}$$

where Ω_i is the cell area at i step for the SWE model (Ω will be the cell volume for a 3D model).

The Courant-Friedrichs-Lewy stability criterion was used to ensure Δt does not exceed its maximum allowable limit, as represented below

$$\Delta t \le C_{FL}\left[\frac{\Omega}{|u_t \cdot \mathbf{s}| + c \cdot |\mathbf{s}|}\right] \tag{19}$$

where $\mathbf{s} = \mathbf{i} + \mathbf{j}$ represents the resultant normal unit vector; c is the wave celerity ($c = \sqrt{gh}$); and C_{FL} is the Courant number, which is limited by $0 < C_{FL} \le 1$. By using smaller values of C_{FL}, the simulation accuracy will be improved; however the computational cost will increase. The combination of CFL criterion with MUSCL-Hancock scheme has been well-tested by Toro [28], hence it is adopted here. In this study, a smaller C_{FL} number of 0.6 was used for the complex multiple obstructions induced flow simulations in Section 6.1; whereas a larger C_{FL} number of 0.8 was found to give stable simulations of the non-uniform flow experiments tested in Sections 6.2 and 6.3.

4.2 *Source Terms Scheme*

An original SGUM source terms treatment scheme proposed by Pu et al. [24] was integrated into this study to simulate the combined operation of $\mathbf{F}$ and $\mathbf{S_T}$ in equation (13). This combination of $\mathbf{F}$ and $\mathbf{S_T}$ in the numerical iterations can improve the numerical accuracy to predict the flow under different turbulence conditions and it has been fully tested on various numerical benchmark problems and experimental data in Pu and Lim [33] and Pu et al. [24] under conditions with and without coupling to the k-ε model, respectively. In this work, the SGUM is used to improve the numerical scheme to treat the combined source terms from SWE and k-ε equations. By applying the SGUM approach, the MUSCL-Hancock scheme in equations (17) – (18) will be altered to

Predictor Step: $$\mathbf{U}_i^{N+1/2} = \mathbf{U}_i^N - \frac{\Delta t}{2\Omega_i}\left(\mathbf{f}_{i+1/2}^N - \mathbf{f}_{i-1/2}^N\right) \tag{20}$$

Corrector Step: $$\mathbf{U}_i^{N+1} = \mathbf{U}_i^N - \frac{\Delta t}{\Omega_i}\left(\mathbf{f}_{i+1/2}^{N+1/2} - \mathbf{f}_{i-1/2}^{N+1/2}\right) \quad (21)$$

where $\mathbf{f} = \mathbf{F} - \Omega \cdot \mathbf{S_T}$.

4.3 *Boundary Conditions*

The double boundary condition, tested in Hu et al. [30], is used for the proposed model, where two extra ghost-cells are utilised outside the computational space domain. There are two kinds of boundary considered, the transmissive and repulsive boundaries. Each of their corresponding boundary vectors $\boldsymbol{U}^B$ can be represented as

Transmissive Boundary: $$\boldsymbol{U}^B = \begin{bmatrix}\phi & \phi u & \phi v & \phi k & \phi\varepsilon\end{bmatrix}^T \quad (22)$$

Repulsive Boundary: $$\boldsymbol{U}^B = \begin{bmatrix}\phi & -\phi u & -\phi v & \phi k & \phi\varepsilon\end{bmatrix}^T \quad (23)$$

The afore-mentioned boundary conditions are updated by using

$$\mathbf{U}_{m+1}^B = \mathbf{U}_m^B \quad (24)$$

$$\mathbf{U}_{m+2}^B = \mathbf{U}_{m-1}^B \quad (25)$$

where m is the last space cell in the computational boundary excluding the ghost cells.

5 Experimental Model

An experimental study was carried out and its measured data were used to validate the proposed numerical model. The descriptions of the experimental instruments and conditions are discussed in the following sub-sections.

5.1 *Experimental Instruments*

A rectangular tilting flume, which has dimensions of length 12m, width 0.45m and height 0.50m, was used in this study. The physical flume was located in the Hydraulic Laboratory at the University of Bradford, where all our experimental tests had been carried out. The upstream end of the flume is connected to the outlet pipe of a water pump, and its downstream end runs into a water tank. The water tank collects the water at downstream end before directing it to the pump to be recirculated into the flume. The flume has glasswalls and a painted steel base. An adjustable gate is located at the downstream end of the flume to control the flow elevation. The flume is also equipped with a track parallel to the flume base for attaching the measurement trolleys, which can be used as the Acoustic Doppler Velocimeter (ADV) or vernier water gauge holder. The flume slope is controlled by a mechanical screw located at the downstream side of the flume, and is equipped with a calibrated scale that indicates the vertical movement of the flume. This calibrated scale allows the tilted vertical distance to be determined up to an accuracy of one millimeter. For detailed experimental descriptions refer to Pu et al. [13] and Pu [25].

The ADV used in this study is equipped with the four-probe-receiver to reduce the noise signal of the measurements as compared to the conventional three-probe-receiver ADV, as the fourth probe provides direct estimation to the instrumentation noise level [34]. It was suggested by Lemmin and Rolland [35] using the investigation on the time-averaged flow field data that the error sources of ADV measurements are generally contributed less than 4% relative error to the velocity measurements. Besides, Hurther and Lemmin [36] also suggested using the investigation on turbulent kinetic energy (TKE), turbulent intensity and Reynolds stress that the four-probe-receiver ADV allows measurements with relative error of less than 10%. Conclusively, these studies constantly suggested the reliability of the four-probe ADV in velocity and turbulence measurements.

5.2 *Experimental Conditions*

A summary of all the hydraulic conditions in different non-uniform flow experiments is presented in Table 1. The velocity measurements were made at four separate streamwise locations (at 3m, 5m, 6m, and 7m from the flume inlet). At each streamwise location, the velocity measurements were made at several vertical positions. Fifteen to twenty-five vertical measurement points were used in a single location depending on the flow condition (presented in Table 1). Each sampling point can have a minimum sampling volume of 1mm^3; however for the measurement points that have low signal-to-noise ratio (SNR), the sampling volume will be increased. In all Test 1 – 4, the velocity measurements were conducted at the ADV sampling frequency of 100Hz for 5 minutes of the sampling time, which this sampling frequency was suggested by Hurther and Lemmin [36] to be sufficient ADV output rate for turbulence measurements.

6 Results and Discussions

The presented numerical model was applied to various flow applications to investigate: (1) its k-ε and SGUM models, and (2) the proposed Kolmogorov k-ε model to reproduce flow turbulence. For validation of the k-ε and SGUM models, a multiple obstructions induced flow outlined in the literature was tested and compared with the proposed model simulation. Then, the non-uniform flow experiments discussed before was used to investigate the combined Kolmogorov k-ε model and its ability to reproduce the flow turbulence structures.

6.1 *Multiple Obstructions Induced Flows*

A multiple obstructions induced flow is used in this section to produce a combination of different constructive and diffusive turbulent eddy effects to test the proposed k-ε SWE model. The experimental measurements of this flow test were conducted by Kabir et al. [37], where the dimensions and sizes of the tested obstructions in the flow are presented in Fig 1. In Kabir et al. test, the full channel had a dimension of 3m length and 0.9m width. However, the channel was bounded by guide-walls to constraint the flow region to 2m length and 0.3m width, where the basic schematic diagram of this bounded region is presented in Fig 1. Three rectangular obstacles (one $l \times b$ and two parallel $L \times c$ blocks) were stationed in the channel against the flow. By referring to Fig 1, some dimensions of the channel and obstacles were fixed as: $w = b = 25\text{mm}$, $L = 200\text{mm}$, and $c = 2.5\text{mm}$. In the experiment, different dimensions of g (50.0, 75.0, 100.0, 125.0, 150.0, 175.0 and 200.0mm) were tested against the $l \times b$ block size with ratio of $l / b = 1.5$. The initial conditions of water depth, streamwise velocity, transverse velocity were set as $h_I = 0.125\text{m}$, $u_I = 0.24\text{m/s}$, and $v_I = 0$, respectively. Using the each settings of the experiment, separate simulations were run until the steady state was reached and the numerical results were compared with the experimental findings.

The simulated flow fields of the two most extreme cases in the range of g, i.e. when $g = 50.0\text{mm}$ and $g = 200.0\text{mm}$, are presented at Figs 2 and 3, respectively. In Fig 2 when $g = 50.0\text{mm}$, one can observe that the turbulent eddies created at the back of $l \times b$ block causing a chaotic flow vorticity behaviour as compared with Fig 3 for $g = 200.0\text{mm}$, where the turbulent eddies occur more tranquilly. When the numerical tests were further run for different ratios of l / b, namely $l / b = 1.0,\ 0.5,\ \text{and}\ 0.3$, we obtained different trend of change for velocity ratio at the flow inlet and outlet (u_i and u_o - the points are presented in Fig 1). Figs 4(a) - (d) show the simulated results of u_i / u_o at different l / b ratios with three different sets of mesh as compared to the experimental measurements by Kabir et al. [37]. From this mesh refinement test, the reasonably converged results has been obtained from coarse mesh (200 × 20) to fine mesh (800 × 20) simulation for all l / b ratio tests.

In Figs 4(a) – (d), the most obvious difference between the numerical predictions and measurements occurs when g / w ratio is small. When the gap g is small (since w fixed as constant), the secondary currents are expected to be more significant in the space between the obstructions, i.e. at the back of $l \times b$ block, compared to the flow through bigger g space. At small g, the flow features a stronger 3D characteristic due to the existing of strong secondary currents, and hence the 2D SGUM-SWE model could not capture it satisfactorily. Furthermore, the disagreement between the 2D SGUM-SWE model with measurements are also expected to be progressively more severe if gap g becomes even smaller. Apart from that, Figs 4(a) – (d) show convincingly that the presented 2D SGUM-SWE model can be utilised as a reasonable tool to simulate the obstructed flow applications, due to its much lower computational cost than the 3D flow models. Moreover, due to the fact that the numerical iteration to resolve the turbulent eddies is usually a very time-consuming process, the SWE-type approach should be seriously considered as to achieve practical engineering simulations.

6.2 *Model Validation on Flow Velocity and Turbulent Kinetic Energy (TKE)*

In this section, the numerical simulations are completed for the physical experiments explained in Section 4, where the mesh size of 480 × 45 (excluding ghost cells) are found to give the most optimum results. Fig 5 shows the depth-averaged streamwise velocity comparisons between the numerical simulations and experimental measurements (for all Test 1 – 4 in Table 1). In the figure, one can observe that Test 1 – 3 had the accelerating characteristics across the streamwise direction from 3m to 7m location, whereas Test 4 had the decelerating characteristics; hence, they are classified as the spatial-accelerating and spatial-decelerating flows, respectively. In detail comparison from the non-uniform flow depth-averaged velocity variation across the streamwise locations, Test 1 and 3 match the measurements better than Test 2 and 4. However, all numerical simulations show reasonably low discrepancies of about 2% with respect to the experimental data. This comparison shows that the proposed simulated velocity represents the measured data well.

After gaining the insight of velocity profile discrepancy, in Fig 6 the depth-averaged numerical simulated TKE is presented and compared with the experimental data for the tests. The plot are produced against a dimensionless water height ratio h_D, which it is defined as below

$$h_D = \frac{h - h_{MI}}{h_{MA} - h_{MI}} \tag{26}$$

where h_{MA} and h_{MI} are the maximum and minimum water depths across the channel, respectively. h_D is a ratio to define the water-head difference in a flow system. In a spatial-accelerating flow, h_D is decreasing from the upstream to downstream in the flow streamwise direction, whereas for a spatial-decelerating flow h_D is increasing.

In Fig 6, the numerical simulations of the non-uniform flow depth-averaged TKEs at different streamwise locations compare well with the experimental measurements. In comparison, the spatial-decelerating flow in Test 4 shows greater energy gradient variations than all other spatial-accelerating flows. This higher energy gradient is caused by the larger bed slope used in the spatial-decelerating flow that creates a bigger flow pressure gradient. Also, due to the steeper bed slope used in Test 4, a higher numerical discrepancy in the simulated TKEs can also be observed. In numerical terms, this larger discrepancy is caused by the increased S_o source terms used in the numerical simulation.

6.3 *Comparison with Boussinesq Model*

In Figs 7 – 8, the numerical predictions of the streamwise and lateral depth-averaged turbulence intensities, $\overline{u'}$ and $\overline{v'}$, respectively, are compared with the measured data for Test 1 – 4. There is no comparison presented involving the vertical turbulence intensity due to the depth-averaged nature of SWE. The numerical predictions of all depth-averaged streamwise and lateral turbulence intensities match our experimental data reasonably. Using an eddy viscosity assumption, the Reynolds stress τ can be modelled by the Boussinesq hypothesis on the diffusive momentum transport. In the wellknown Boussinesq model, suggested by Launder and Spalding [38] as a combination with the k-ε model, each element of Reynolds stress τ_{ij} is related to the TKE and strain rate of mean flow as follows

$$\frac{\tau_{ij}}{\rho} = 2\nu_t S_{ij} - \frac{2}{3}\delta_{ij}k \tag{27}$$

where ρ is the flow density; $S_{ij} = 0.5\left(\partial u_i / \partial x_j + \partial u_j / \partial x_i\right)$ is the element of mean strain rate; and δ_{ij} is the Kronecker delta. Numerical simulations using equation (27) is employed here to compare with the proposed Kolmogorov k-ε model for reproducing the measured flow Reynolds stress. In Fig 9, we can observe that both proposed and Boussinesq models simulate the measured Reynolds stress with satisfactory correspondence.

Table 2 presents the proposed model numerical discrepancies of Test 1 – 4 by benchmarking using the experimental data. The table shows that $\overline{u'}$, $\overline{v'}$ and $\tau = -\overline{u'v'}$ have the averaged discrepancies of 2.33%, 2.23% and 3.68%, respectively, across all tests, which they outline the accuracy of the proposed model to reproduce the flow turbulence structures. In comparison, the streamwise and lateral turbulence intensities show similar averaged discrepancy, which they are both lower than that of their correlative Reynolds stress. However, all their discrepancies are significantly low, and that shows the proposed model capability. These comparisons further strengthen the idea of combining the Kolmogorov approach into the k-ε SWE model to propose a computationally cost-saving method for the practical simulation of RANS turbulence structures.

7 Conclusions

A numerical model has been proposed to combine the shallow water model with k-ε equations to study the flow turbulence structures. The Kolmogorov K41 scaling law was utilised to compute the flow velocity fluctuations in the combined k-ε SWE model, in order to determine the flow turbulence intensities in different directions and Reynolds stress. The model was also further improved in its source terms numerical representation by using a SGUM approach. Literature studies and laboratory flow experiments, which were performed under the non-uniform flow conditions, were used to validate the proposed numerical model.

The comparison with literature showed that the proposed k-ε and SGUM models were well-combined to reproduce the flow characteristics of the investigated multiple-obstructions induced flow. In our experiments, the numerical and experimental comparisons were accomplished in the flow velocity, TKE, streamwise and lateral turbulence intensities as well as Reynolds stress to fully investigate the proposed model representation of the flow turbulence structures. Besides, a standard Boussinesq model was also utilised to compare with our numerical and experimental Reynolds stress results, where good agreement was observed in between one another.

All the comparison results showed that the presented model captured the experimental flow characteristics reasonably well in all the considered flows. All of these comparisons proved that the proposed k-ε SWE numerical model was capable to represent the actual flow turbulence structures after combining with the Kolmogorov K41 scaling model to perform the computationally efficient calculation in 2D. The finding of this study also proves that the Kolmogorov model should be given attention by future researches as an achievable approach to resolve the computationally demanding flow turbulence.

Acknowlegdements

The author acknowledges the support of the Major State Basic Research Development Program (973 program) of China (No. 2013CB036402). The author would also like to thank the associate editor and four anonymous reviewers for their insightful comments to improve the paper.

References

1. Liu X, Garcia MH. Three-dimensional numerical model with free water surface and mesh deformation for local sediment scour. J Hydraul Eng 2008;134(4):203-217.
2. Bihs H, Olsen NRB. Numerical modeling of abutment scour with the focus on the incipient motion on sloping beds. J Hydraul Eng 2011;137(10):1287-1292.
3. Harlow FH, Welch JE. Numerical calculation of time-dependent viscous incompressible flow. Phys Fluids 1965;8:2182-2189.
4. Lin P, Liu PFL. A numerical study of breaking waves in the surf zone. J Fluid Mech 1998;359:239-264.
5. Zhou JG, Stansby PK. An arbitrary Lagrangian-Eulerian σ (ALES) model with non-hydrostatic pressure for shallow water flows. Comput Meth Appl Mech Eng 1999;178:199-214.
6. Iafrati A, Di Mascio A, Campana EF. A level set technique applied to unsteady free surface flows. Int J Numer Meth Fluids 2001;35:281-297.
7. Chu V. Shear instability, wave and turbulence simulations using the shallow-water equations. J Hydro-environ Res 2010;3(4):173-178.
8. Talstra H. Large-scale turbulence structures in shallow separating flows. [PhD Thesis], Delft University of Technology, the Netherlands; 2011.
9. Shih TH, Zhu J, Lumley JL. Calculation of wall-bounded complex flows and free shear flows. Int J Numer Methods in Fluids 1996;23(11):1133–1144.
10. Rodi W. Turbulence models and their application in hydraulics. IAHR Monograph, Taylor and Francis, New York; 1993.
11. Cea L. An unstructured finite volume for unsteady turbulent shallow water flow with wet-dry fronts: numerical solver and experimental validation. [PhD Thesis], Universidad De La Coruna, Spain; 2005.
12. Jiang CB, Yang C, Liang DF. Computation of shallow wakes with the fractional step finite element method. J Hydraul Res 2009;47(1):127-136.

13. Pu JH, Shao S, Huang Y. Numerical and experimental turbulence studies on shallow open channel flows. J Hydro-environ Res 2014;8:9-19.
14. Cea L, Puertas J, Vazquez-Cendon ME. Depth average modelling of turbulent shallow water flow with wet-dry fronts. Arch Comput Meth Eng 2007;14(3):303-341.
15. Cea L, Pena L, Puertas J, Vazquez-Cendon ME, Pena E. Applications of several depth-averaged turbulence models to simulate flow in vertical slot fishways. J Hydraul Eng 2007;133(2):160-172.
16. Kolmogorov AN. The local structure of turbulence in incompressible viscous fluid for very large Reynolds number. C R Acad Sci URSS 1941;30:301-305.
17. Kolmogorov AN. On the degeneration of isotropic turbulence in an incompressible viscous fluid. C R Acad Sci URSS 1941;31:538-541.
18. Kolmogorov AN. Dissipation of energy in isotropic turbulence. C R Acad Sci URSS 1941;32:19-21.
19. Nezu I, Nakagawa H. Turbulent open-channel flows. IAHR Monograph, A. A. Balkema, the Netherlands; 1993.
20. Hunt JCR, Eames I, Westerweel J, Davidson PA, Voropayev S, Fernando J, Braza M. Thin shear layers – the key to turbulence structure? J Hydro-environ Res 2010;4(2):75-82.
21. Caselles V, Donat R, Haro G. Flux-gradient and source-term balancing for certain high resolution shock-capturing schemes. Comput Fluids 2009;38:16-36.
22. Fernandez-Nieto ED, Marin J, Monnier J. Coupling superposed 1D and 2D shallow-water models: source terms in finite volume schemes. Comput Fluids 2010;39:1070-1082.
23. Xia X, Liang Q, Pastor M, Zou W, Zhuang YF. Balancing the source terms in a SPH model for solving the shallow water equations. Adv Water Resour 2013;59:25-38.
24. Pu JH, Cheng NS, Tan SK, Shao S. Source terms treatment of SWEs using surface gradient upwind method. J Hydraul Res 2012;50(2):145-153.

25. Pu JH. Efficient finite volume numerical modelling and experimental study of 2D shallow water free surface turbulent flows. [PhD Thesis], University of Bradford, UK; 2008.
26. Cea L, Puertas J, Vazquez-Cendon ME. Depth average modelling of turbulent shallow water flow with wet-dry fronts. Arch Comput Meth Eng 2007;14(3):303-341.
27. Younus M, Chaudhry MH. A depth-averaged k-ε turbulent model for the computation of free-surface flow. J Hydraul Res 1994;32(3):415-444.
28. Toro EF. Riemann solvers and numerical methods for fluid dynamics: a practical introduction. Springer-Verlag, Germany; 1999.
29. Mingham CG, Causon DM. Calculation of unsteady bore diffraction using a high resolution finite volume method. J Hydraul Res 2000;38(1):49-56.
30. Hu K, Mingham CG, Causon DM. A mesh patching method for finite volume modelling of shallow water flow. Int J Numer Meth Fluids 2006;50(12):1381-1404.
31. Toro EF, Garcia-Navarro P. Godunov-type methods for free-surface shallow flows: a review. J Hydraul Res 2007;45(6):736-751.
32. van Leer B. Towards the ultimate conservative difference scheme II. Monotonicity and conservation combined in a second order scheme. J Comput Phys 1974;14:361-370.
33. Pu JH, Lim SY. Efficient numerical computation and experimental study of temporally long equilibrium scour development around abutment. Environ Fluid Mech 2014;14:69-86.
34. Lohrmann A, Malzone C. Vectrino – Micro ADV comparison. Nortek Technical Note No. TN-022; 2004:1-8.
35. Lemmin U, Rolland T. Acoustic velocity profiler for laboratory and field studies. J Hydraul Eng 1997;123(12):1089-1098.
36. Hurther D, Lemmin U. A correction method for turbulence measurements with a 3D acoustic Doppler velocity profiler. J Atmos Oceanic Tech 2001;18:446-458.

37. Kabir MA, Khan MMK, Bhuiyan MA. Flow phenomena in a channel with different shaped obstructions at the entrance. Fluid Dyn Res 2004;35:391-408.
38. Launder BE, Spalding DB. The numerical computation of turbulent flows. Comput Method Appl Mech Eng 1974;3:269-289.

Table 1. Summary of experimental measurement conditions

Test No.	**Slope ($\times 10^{-3}$)**	**Discharge (m^3/s)**	**Flow Characteristics**	**No. of Measuring Points in a Single Location**
1	Flat	0.0270	Spatial-Accelerating	20
2	Flat	0.0315	Spatial-Accelerating	22
3	Flat	0.0360	Spatial-Accelerating	25
4	2.50	0.0315	Spatial-Decelerating	15–19

Table 2. Average numerical simulation discrepancies of the depth-averaged $\overline{u'}$, $\overline{v'}$ and τ (benched by experimental measurements) in Figures 7 – 9 (for Test 1 – 4)

Turbulence Structures	**Averaged Numerical Discrepancies (in %)**			
	Test 1	**Test 2**	**Test 3**	**Test 4**
$\overline{u'}$	2.3	2.4	2.1	2.5
$\overline{v'}$	2.6	2.5	2.0	1.9
$\tau = -\overline{u'v'}$	2.9	4.1	4.0	3.7

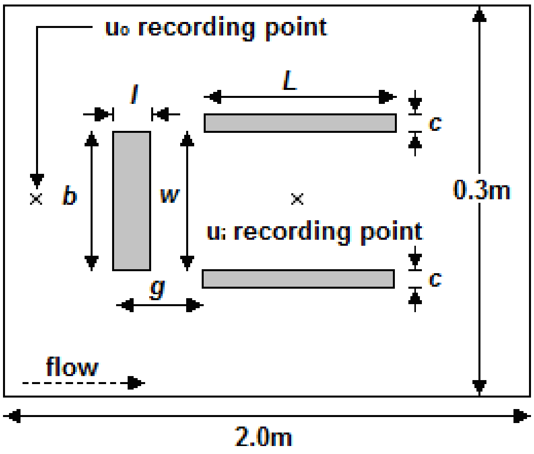

Figure 1. Layout of multiple obstructions induced flow

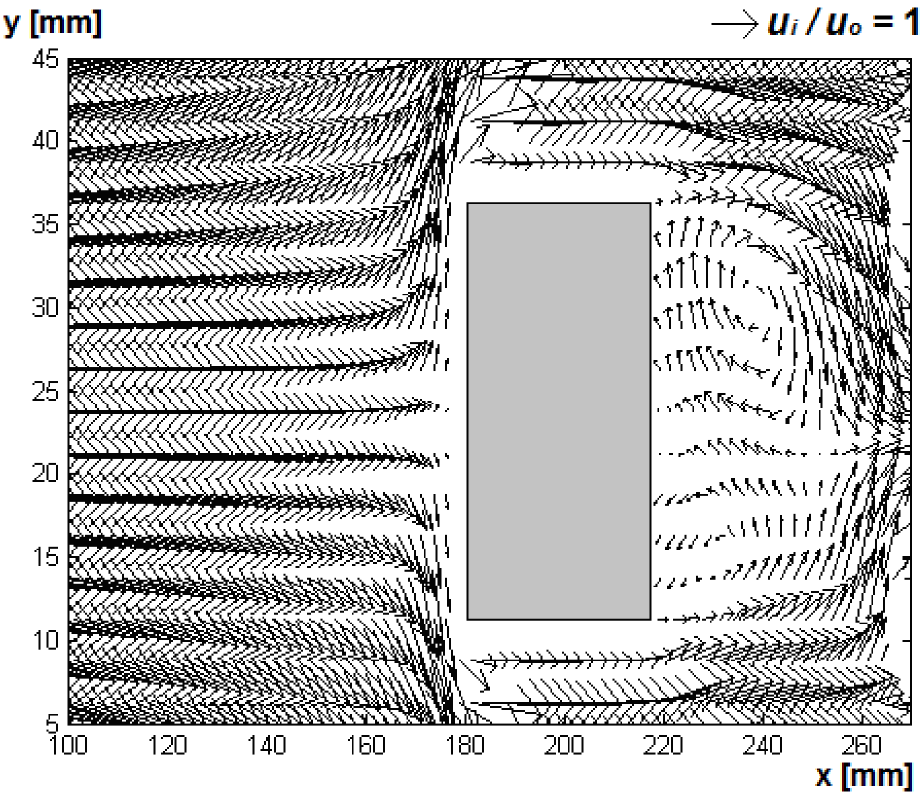

Figure 2. Flow field around $l \times b$ block at dimensions $g = 50.0\text{mm}$ and $l/b = 1.5$

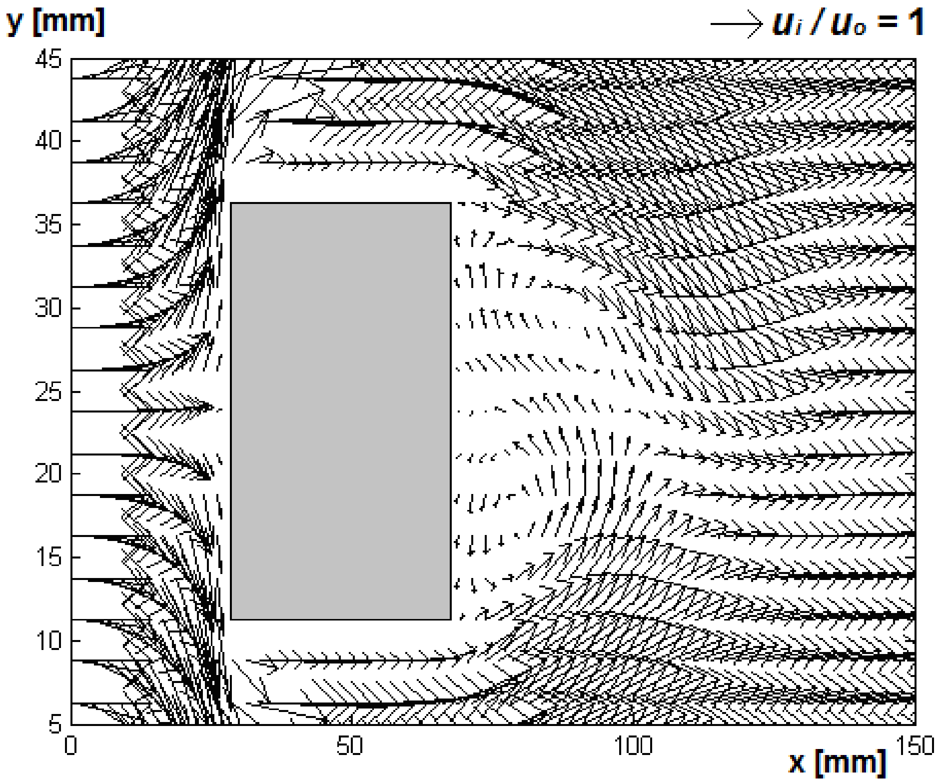

Figure 3. Flow field around $l \times b$ block at dimensions $g = 200.0\text{mm}$ and $l/b = 1.5$

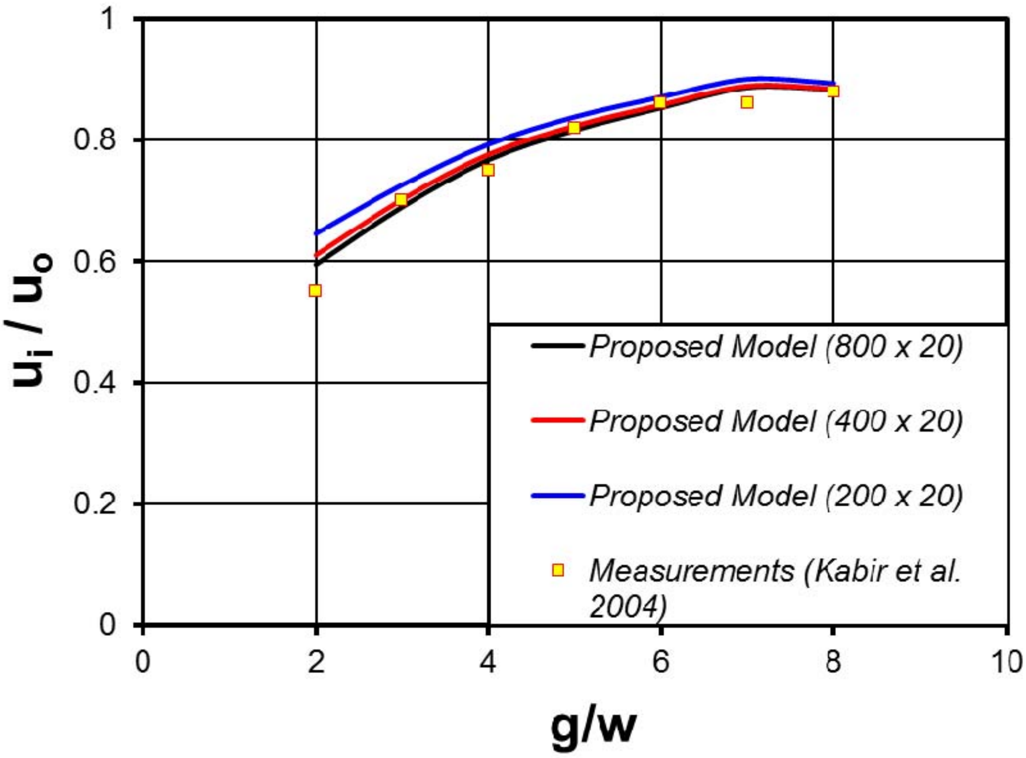

Figure 4(a). u_i / u_o comparison when $l / b = 1.5$

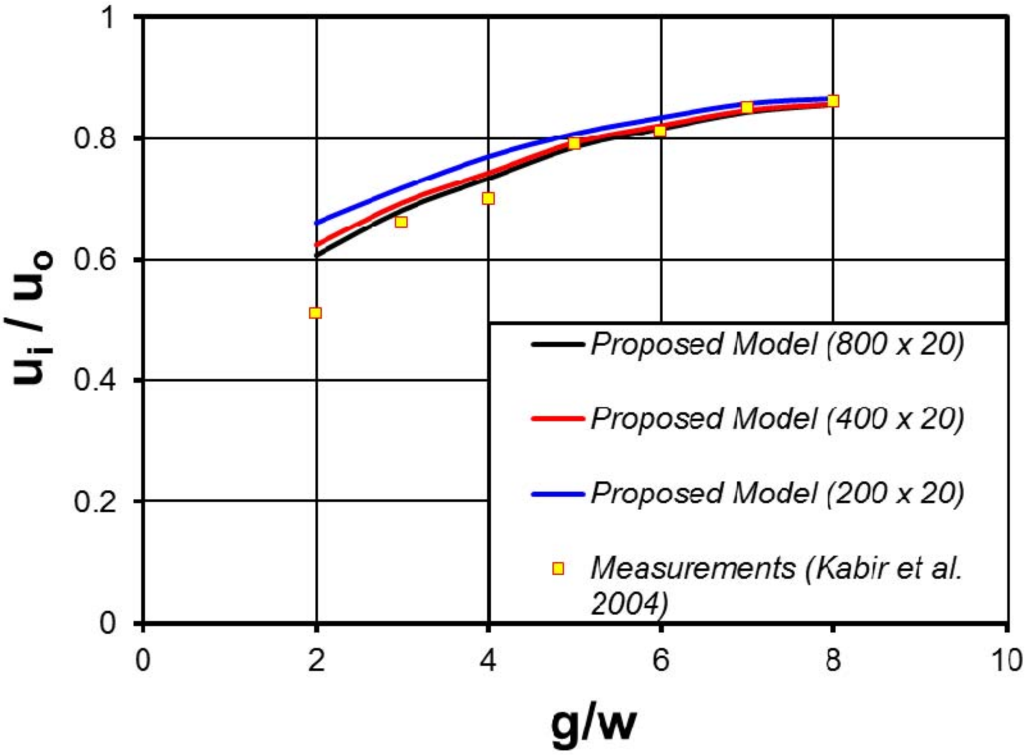

Figure 4(b). u_i / u_o comparison when $l / b = 1.0$

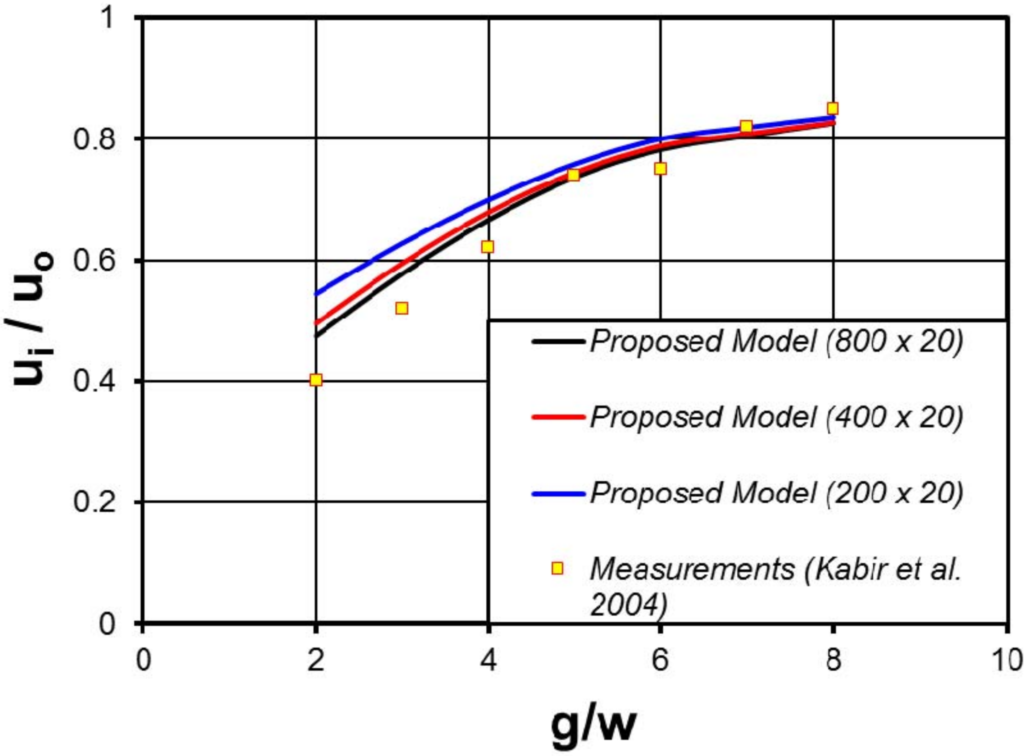

Figure 4(c). u_i / u_o comparison when $l / b = 0.5$

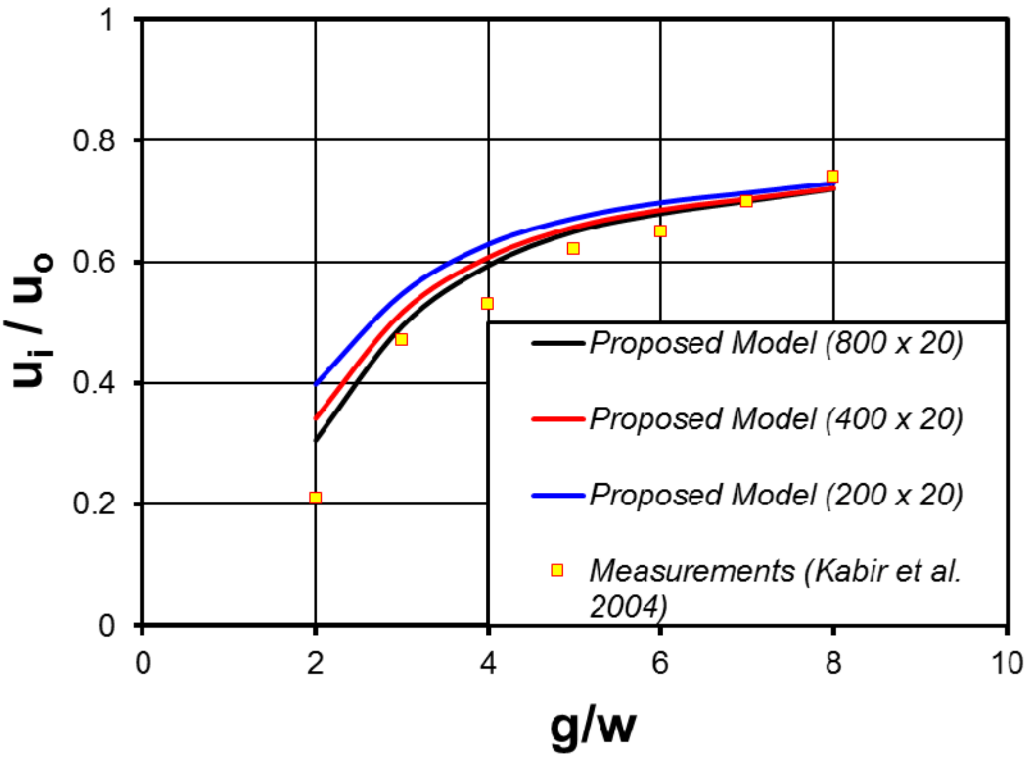

Figure 4(d). u_i / u_o comparison when $l / b = 0.3$

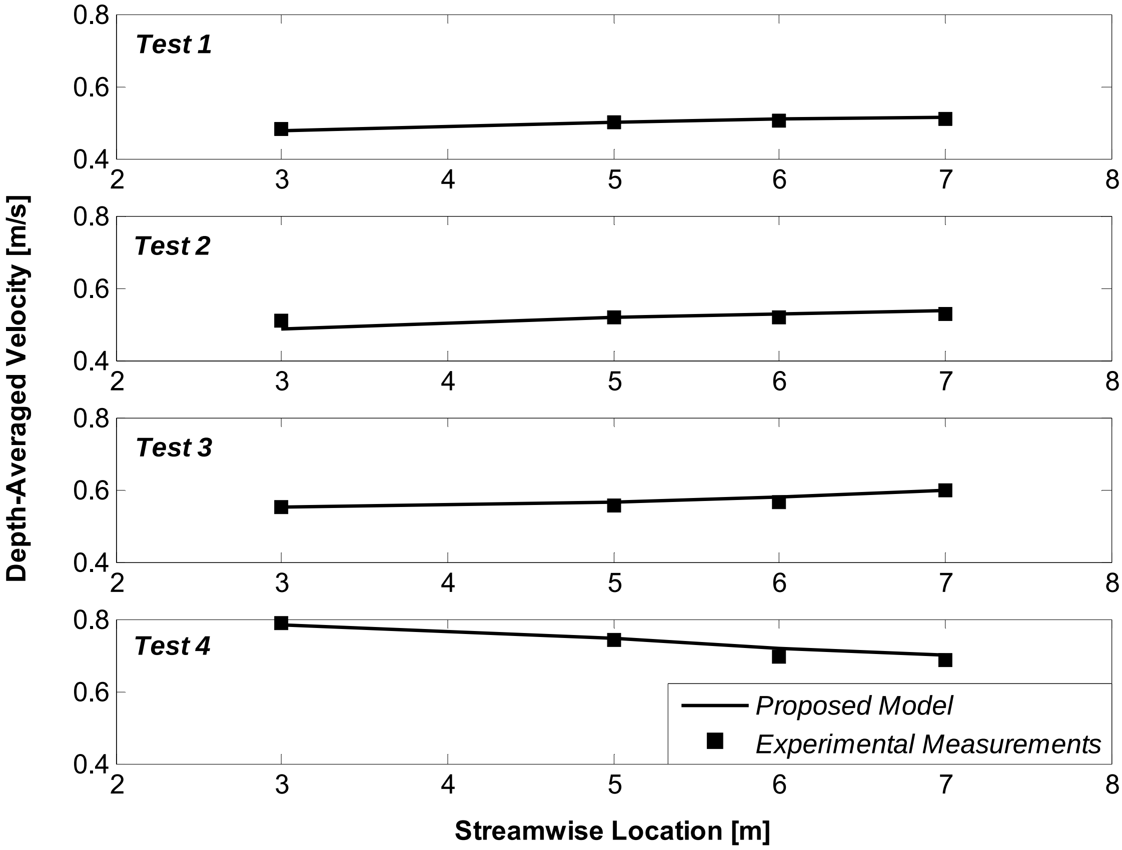

Figure 5. Comparison of numerical simulated and experimental measured depth-averaged velocities for different tests

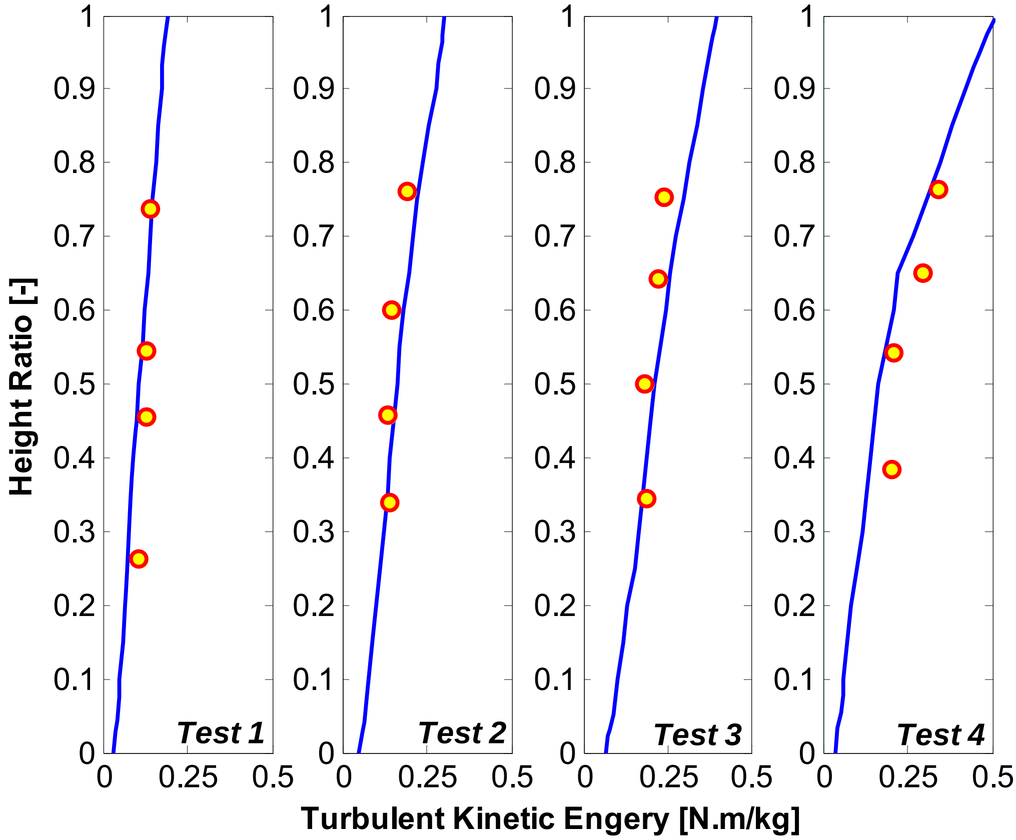

Figure 6. TKE against the water height ratio h_D (symbol – experimental data, blue solid line – proposed numerical simulations)

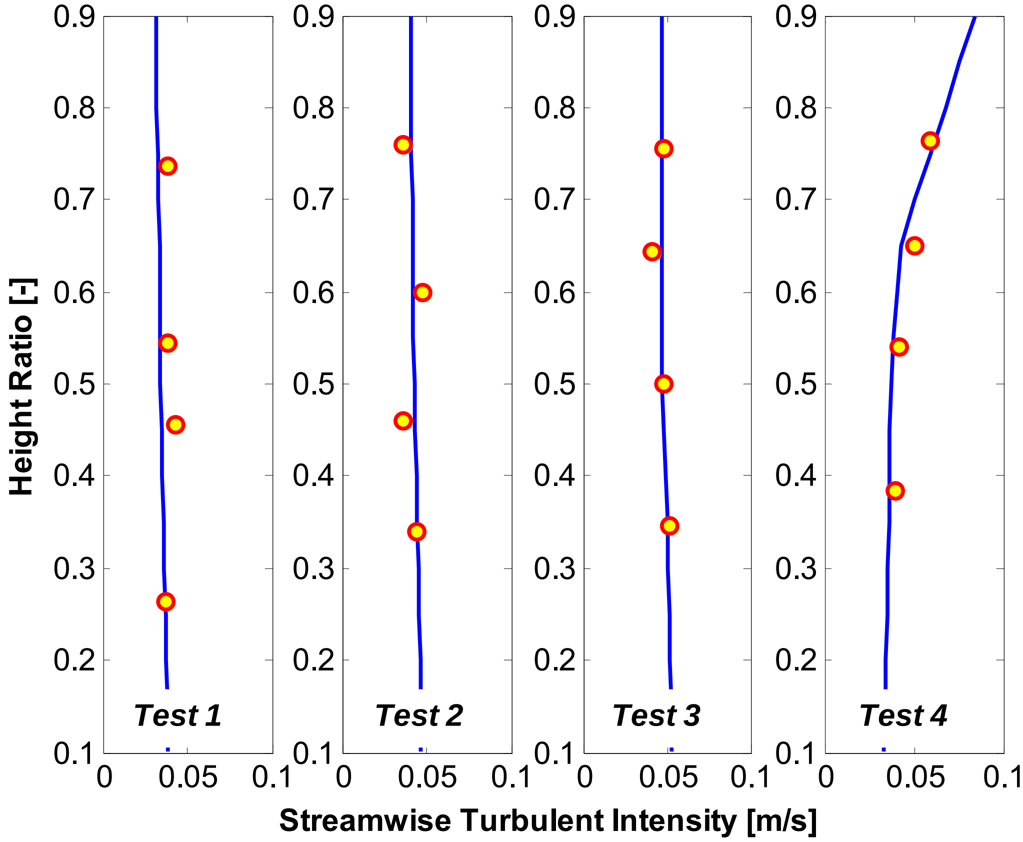

Figure 7. Streamwise turbulence intensity against the water height ratio h_D (symbol – experimental data, blue solid line – proposed numerical simulations)

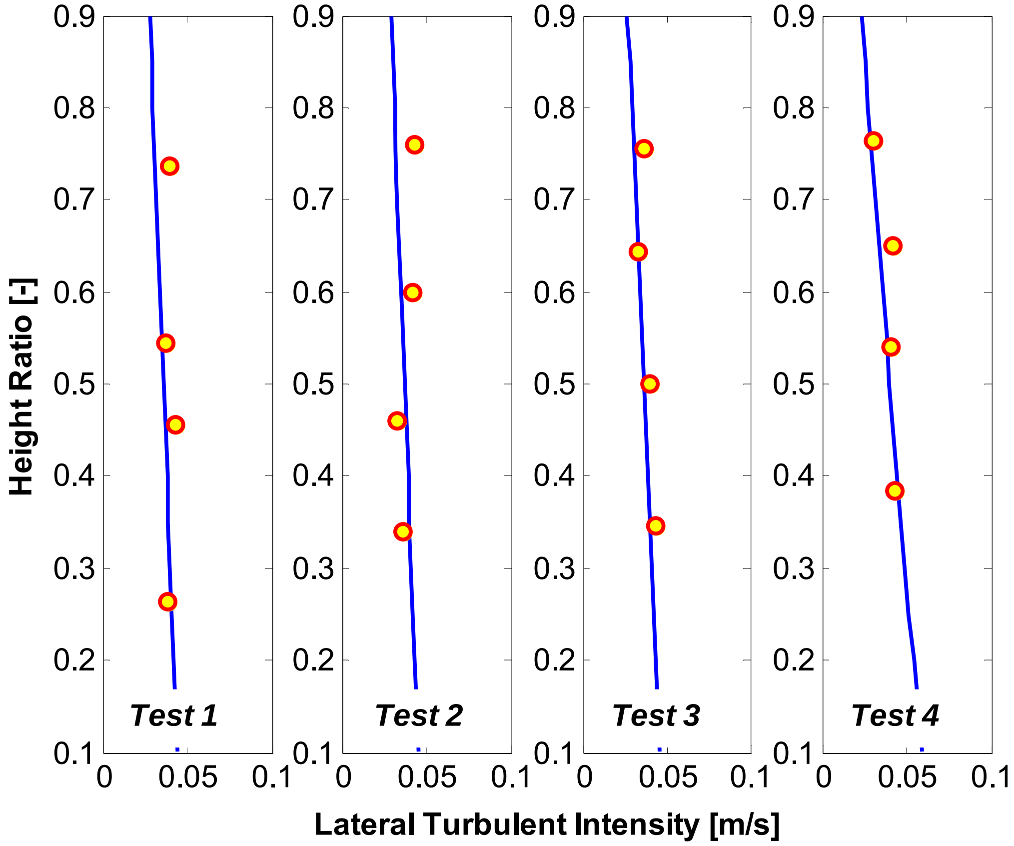

Figure 8. Lateral turbulence intensity against the water height ratio h_D (symbol – experimental data, blue solid line – proposed numerical simulations)

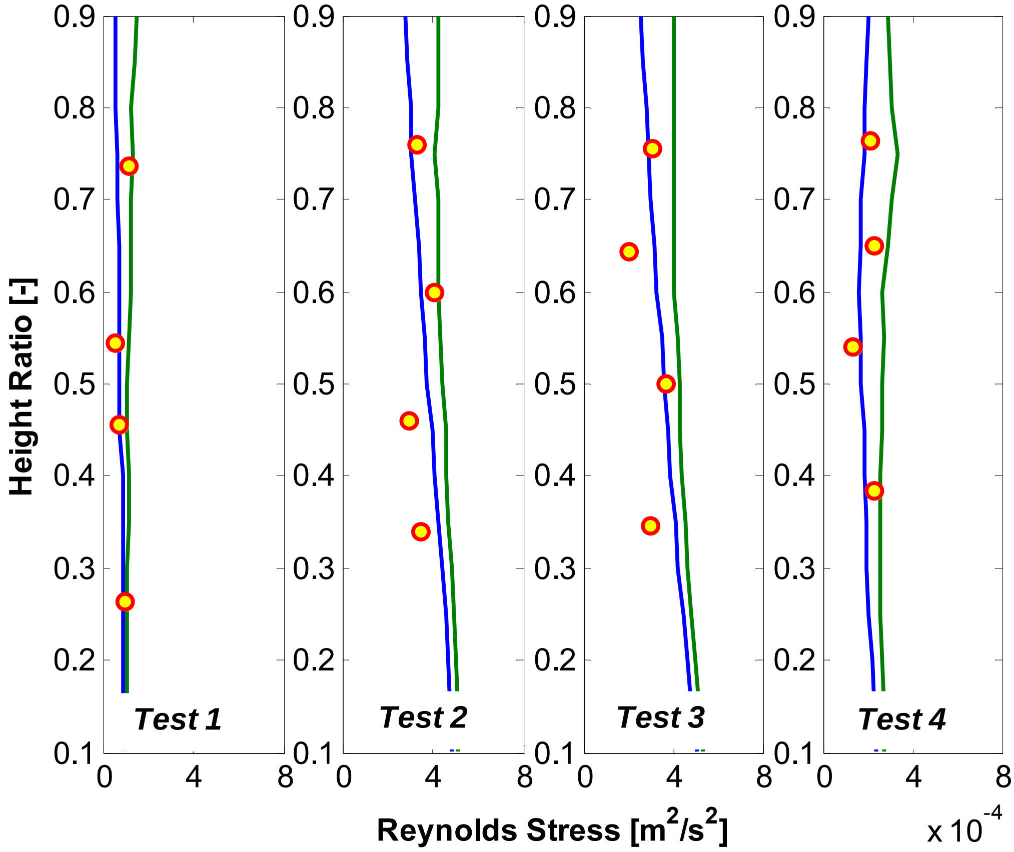

Figure 9. Reynolds stress against the water height ratio h_D (symbol – experimental data, green solid line – Boussinesq model simulations, blue solid line – proposed numerical simulations)